ACS Photonics

pubs.acs.org/journal/apchd5 Article

Efficient Photonic Integration of Diamond Color Centers and Thin-Film Lithium Niobate

Daniel Riedel,* Hope Lee, Jason F. Herrmann, Jakob Grzesik, Vahid Ansari, Jean-Michel Borit, Hubert S. Stokowski, Shahriar Aghaeimeibodi, Haiyu Lu, Patrick J. McQuade, Nicholas A. Melosh, Zhi-Xun Shen, Amir H. Safavi-Naeini, and Jelena Vučković*

Cite This: https://doi.org/10.1021/acsphotonics.3c00992 Read Online

ACCESS | Metrics & More | Article Recommendations | Supporting Information

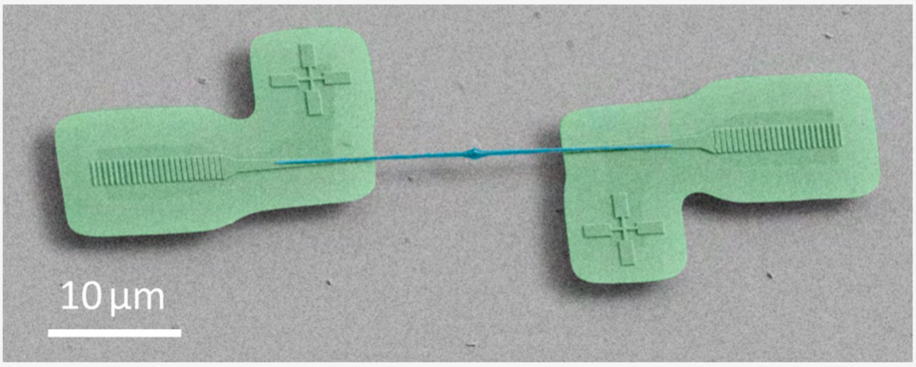

ABSTRACT: On-chip photonic quantum circuits with integrated quantum memories have the potential to radically advance hardware for quantum information processing. In particular, negatively charged group-IV color centers in diamond are promising candidates for quantum memories as they combine long storage times with excellent optical emission properties and an optically addressable spin state. However, as a material, diamond lacks the many functionalities needed to realize scalable quantum systems. Thin-film lithium niobate (TFLN), in contrast, offers a number of useful photonic nonlinearities, including the electro-optic effect, piezoelectricity, and capabilities for periodically poled quasi-phase matching. Here, we present the highly efficient heterogeneous integration of diamond nanobeams containing negatively charged silicon-vacancy (SiV) centers with TFLN waveguides. We observe greater than 90% transmission efficiency between the diamond nanobeam and the TFLN waveguide on average across multiple measurements. By comparing saturation signal levels between confocal and integrated collection, we estimate a more than 10-fold increase in photon emission channeled into TFLN waveguides versus that channeled into out-of-plane collection channels. Our results constitute a key step for creating scalable integrated quantum photonic circuits that leverage the advantages of both diamond and TFLN materials.

KEYWORDS: *heterogeneous integration, thin-film lithium niobate, diamond, quantum photonics, silicon-vacancy center, color centers*

INTRODUCTION

Optically addressable solid-state spin qubits are promising building blocks for scalable quantum networking applications.[1,2] Among these, diamond color center defects are leading candidates for advancing quantum networks. Long-lived ^{13}C nuclear spins in diamond can be harnessed as quantum memories,[3,4] while nitrogen-vacancy centers have been used to demonstrate a multinode quantum network[5] and quantum teleportation between non-neighboring nodes.[6] Further progress hinges on the efficient integration of color centers into photonic structures to enhance the spin-photon interface without introducing excessive noise.[7−9]

Negatively charged group-IV color centers benefit from structural inversion symmetry, which, to the first order, shields the local spin structure from nearby electric field noise introduced during nanofabrication.[10,11] In addition, this family of color centers consistently exhibits high Debye−Waller factors, leading to strong emission into the zero phonon line (ZPL).[12] These features, in combination with the efficient coupling to nanophotonic cavities, have enabled the demonstration of memory-enhanced quantum communication[13] and the generation of streams of indistinguishable photons,[14]

Received: July 18, 2023
Revised: November 9, 2023
Accepted: November 13, 2023

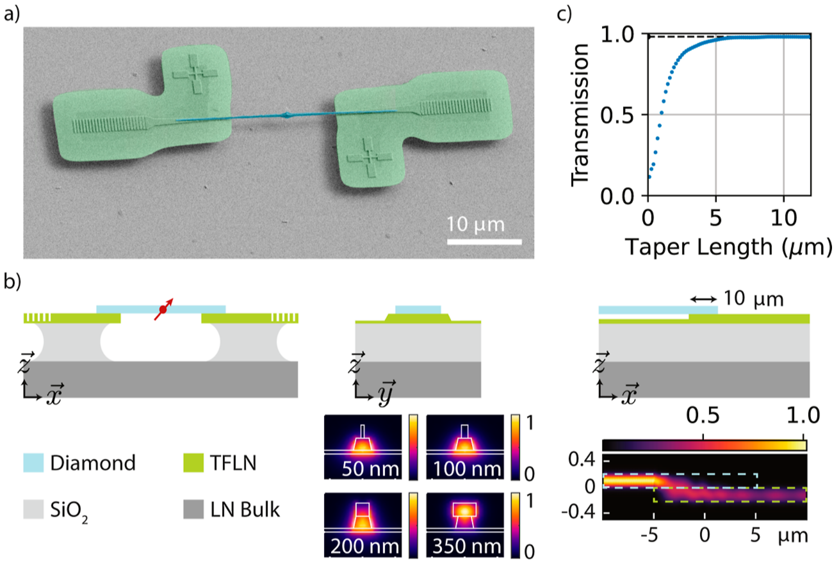

Figure 1. Structure for adiabatic transfer of light from diamond to TFLN: (a) False-colored scanning electron microscopy image of the fully integrated nanobeam device, with a few nanometers of Au sputtered atop for charge dissipation. Green corresponds to the TFLN, while blue represents the diamond nanobeam. As evident from the image, the TFLN slab around the device has been etched, revealing the buried oxide layer, which is partially undercut, leaving a partially suspended TFLN platform. (b) Schematics and simulations of the device. (Left) Side profile. (Mid) Simulated cross-section of the inverse taper region. A diamond nanobeam rests on TFLN on an insulator, with a buried oxide layer. The four images depict COMSOL simulations of the fundamental TE mode of the hybridized waveguide, demonstrating adiabatic mode transfer between the diamond and TFLN. The width of the diamond waveguide is given in each inset, with the TFLN waveguide top width fixed at 200 nm. Each plotted region is 1.2 μm wide and 1 μm tall and depicts the electric field norm, normalized to its maximum. (Right) Length-wise cross-section schematic of the adiabatic taper simulation. The taper is simulated with a 10 μm overlap between the diamond nanobeam taper and the TFLN taper. The lower image depicts a Lumerical simulation of the normalized electric field intensity with outlines indicating the approximate locations of the diamond and TFLN waveguides. All *x*- and *y*-axis dimensions are in microns. (c) Lumerical FDTD simulations of transmitted power between the diamond and TFLN with swept taper lengths. The maximum simulated taper transmission efficiency is ~98%, indicated by the dashed black line.

rendering silicon-vacancy (SiV) centers a prime candidate for quantum networking applications.

However, scalable monolithic fabrication of diamond photonic integrated circuits (PICs) has not been implemented, and complex diamond PICs are precluded by the absence of second-order nonlinearities. To overcome these challenges, heterogeneous integration with mature nanophotonic material platforms is a promising approach.[15−26] Thin-film lithium niobate (TFLN) offers many advantages over alternative photonic materials via large $\chi^{(2)}$ nonlinearity. This enables many applications, including strong electro-optic modulation and frequency conversion,[27−30] piezoelectric transduction,[31,32] and periodic poling for quasi-phase matching and nonlinear frequency conversion.[33,34]

Here, we demonstrate efficient heterogeneous integration of a diamond nanobeam featuring incorporated SiV color centers with a TFLN platform using a mechanical pick-and-place approach.[15,35−37] By precisely placing double-tapered diamond nanobeams, we demonstrate the bridging of a gapped TFLN waveguide with a diamond-to-LN transmission efficiency of 92 ± 11% per facet at 737 nm, corresponding to the SiV ZPL wavelength, averaged across multiple measurements. We find an approximately 2-fold improvement in ZPL photon extraction via integrated TFLN collection channels compared with that via out-of-plane collection from the same device. By taking into consideration measured grating coupler efficiencies, we can infer a more than 10-fold improvement in photon channeling into the TFLN waveguide compared with that into confocal collection channels. Our results demonstrate a crucial step toward the incorporation of high-quality diamond spin qubits into a scalable nonlinear photonics platform.

RESULTS

Device Fabrication and Transfer. Our device consists of a diamond double-tapered nanobeam with incorporated SiV centers bridging a gapped, undercut TFLN waveguide, as imaged in Figure 1a. The SiV color centers are generated during a chemical vapor deposition overgrowth process on an electronic grade bulk single-crystalline diamond. We fabricate the diamond nanobeams using the well-established quasi-isotropic etching technique following the procedures outlined in refs 11, 35, and 38−40 (see the Supporting Information). Our diamond devices consist of a 10 μm long rectangular nanobeam with 10 μm tapers at each end, for a total length of 30 μm. The nanobeam has a target thickness of ~200 nm, and its width is tapered from ~350 to ~50 nm at the taper end. The device is anchored to the bulk substrate via a thin tether, around which the nanobeam is widened slightly to reduce scattering effects of the tether on optical transmission.

The TFLN waveguides are fabricated following the techniques demonstrated in ref 29. We first pattern a negative resist mask atop a lithium niobate-on-insulator (LNOI) substrate using electron beam lithography. We then employ Ar ion milling to etch the waveguides. A second photolithography mask and ion mill step are used for additional removal of the TFLN slab to expose the buried oxide layer of the LNOI. An additional acid cleaning procedure partially etches this oxide, thereby undercutting the waveguide sockets. The completed TFLN waveguides are approximately 190 nm thick atop an approximately 60 nm thick slab and ∼1 μm wide, which assists in the placement of the diamond nanobeam by allowing for a larger margin of alignment error (Figure 1b). The waveguides adiabatically taper to ∼100 nm over a length of 5 μm. A 15 μm gap is left between the two waveguides to serve as a "socket" for a diamond nanobeam. Each waveguide ends in a grating optimized to couple 737 nm light to and from the device (Supporting Information).

Following fabrication, the diamond nanobeam is transferred via pick-and-place to the TFLN socket. The mechanical transfer process is carried out using a home-built micromanipulation setup equipped with confocal imaging capabilities and dual tungsten "cat-whisker" needles, each with a ∼ 70 nm tip radius. To assist with the mechanical breakoff process, the holding tethers are partially cut via focused ion beam (FIB) etching. During transfer, the precise orientation of the nanobeam can be controlled with the dual needles, while the TFLN chip is mounted on a combination of translation and rotation stages. After careful positioning, strong adhesion between the diamond nanobeam and the TFLN via van der Waals forces allow us to remove the attached needle by pulling it down into the etched trench between the TFLN waveguides. Ultimately, the diamond nanobeam tapers are positioned inversely to the LN "socket" tapers, enabling high-efficiency adiabatic transfer of light between the TFLN waveguide and the diamond nanobeam, as shown in Figure 1b,c. From the simulations presented in Figure 1c, we expect a theoretical upper bound on the single-taper transmission efficiency of approximately 98%.

Optical Characterization of Devices. We characterize our device in a closed-cycle Montana cryostat at a temperature of ∼5 K utilizing a home-built confocal microscopy setup consisting of two distinct access arms. We refer to these collection arms as the confocal and transmission paths. The transmission path can be removed from the apparatus by withdrawing the dichroic beamsplitter just before the cryostat. The full measurement apparatus is schematically depicted in Figure 2.

Transmission. As a first step, we measure transmission through our device, using the TFLN grating couplers to characterize the single-taper transmission efficiency between the diamond and TFLN. Using the transmission measurement path, we send a narrow-band laser source through one grating coupler and measure the output power through the other. The input laser power is calibrated via a fiber beamsplitter and a photodiode at the input. The output transmitted light is coupled into a single mode fiber and routed to a second photodiode. We sweep the Ti/sapphire laser excitation from 700 to 780 nm in intervals of 5 nm, with a separate measurement performed at 737 nm specifically, as demonstrated in Figure 3b. Direct transmission through the device at 737 nm is determined to be 2.8 ± 0.4% from single-mode fiber to single-mode fiber, averaged over four distinct measurements. We then shift the stage to a "control" device, consisting of a fully connected (i.e., no taper or gap) TFLN waveguide with nominally identical grating couplers, while keeping the excitation and collection alignment fixed. Transmission through the control device (similarly averaged across four distinct measurements) is 3.3 ± 0.5%. We optimize the transmission through this control device solely by translating the device around beneath the excitation/collection paths. These transmission values are not corrected for any additional losses such as the finite transmission efficiency of various optical elements (objective and silver mirrors) and nonperfect

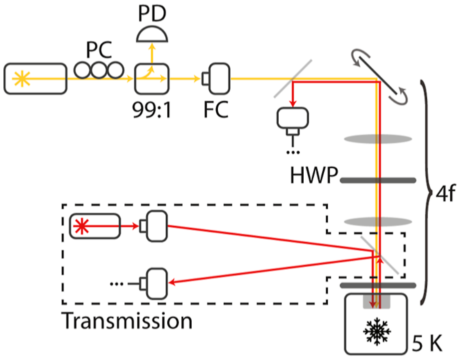

Figure 2. Schematic of the measurement setup for optical characterizations. "PC" (polarization controller), "PD" (photodiode), "99:1" (99%: 1% beamsplitter), "4f" (4-f imaging path, lengths not to scale), "HWP" (half-wave plate), "FC" (fiber-to-free space coupler), and "5 K" (cryostat at 5 Kelvin). The dashed box indicates the removable dichroic beamsplitter and transmission path. We achieve spatial separation of the two transmission collection spots via a D-shaped mirror.

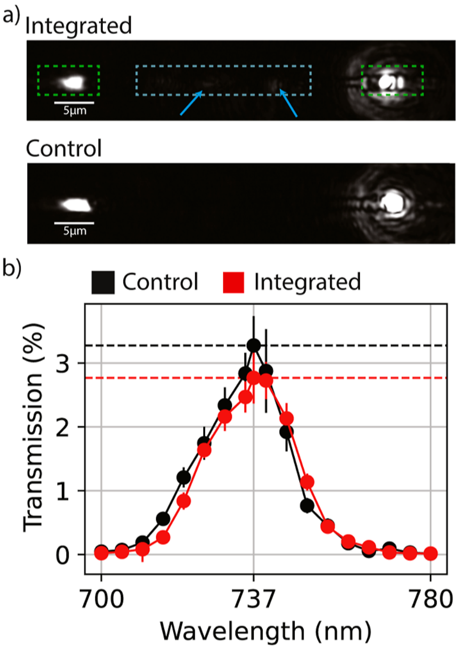

Figure 3. Transmission characterization through the integrated device. (a) (top) Camera image of efficient transmission of narrowband laser light through the integrated device, indicating high taper efficiency at the diamond/TFLN interface. Minimal scattering (indicated by arrows) at the contact points and along the device further demonstrates the efficient adiabatic transfer of light. The diamond nanobeam and grating coupler locations are indicated by the blue and green dashed boxes, respectively. (bottom) Camera image for comparison of the fully connected TFLN control device. Images were taken at 20 ms camera exposure. (b) Average transmission through the integrated diamond−TFLN device (red) and a fully connected TFLN "control" device (black). Error bars depict the standard deviation by averaging four measurements over two separate cooldowns of the devices. The dashed black and red lines indicate the transmission at 737 nm for the control and integrated devices, respectively.

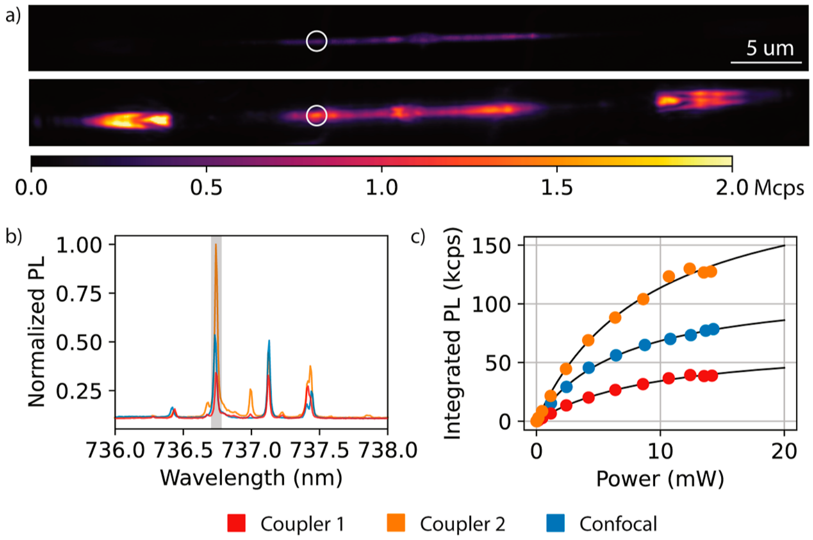

Figure 4. Color center: PL characterizations. (a) Confocal laser scans with confocal collection (top) and stationary coupler collection (bottom). The coupler collection PL scan presented is obtained by counting photon arrivals from the couplers in parallel, with each avalanche photodiode collecting emission from one grating coupler. Over an integration period, these simultaneous counts are summed to yield the total photons collected from both grating couplers. Excitation for both were provided confocally, and scanning is performed utilizing a galvanometer mirror and 4f setup. The white circle in each scan indicates the location of confocal excitation for panels (b) and (c). (b) Normalized PL spectrum, overlaid with confocal and both coupler collected spectra. The gray region indicates the postprocessed "filtered" wavelength range, determined by fitting the spectra to multiple Lorentzian peaks and identifying the FWHM of the selected emission peak for a single emitter. (c) Saturation curves for each collection configuration. CPS for each power and configuration is determined by integrating the number of counts collected in a spectrum within the FWHM ranges identified by the Lorentzian fit. PL spectra were each integrated for 2.5 s. The black trend lines represent a standard power saturation fit. Error bars for each data point were calculated using Poissonian photon statistics but are smaller than data markers.

alignment. Measuring the control device yields a lower bound for the single-mode grating coupler efficiency of 17.3 ± 1.2%, in agreement with grating coupler simulations (Supporting Information). Comparing the transmission values of our device with the control device allows the diamond−LN transfer efficiency to be inferred. Importantly, the control device is measured during the same cooldown using the exact same external optical alignment of the excitation and collection arms; only the sample is displaced between measurements. Attributing all additional losses in the device to the adiabatic taper facets, we conclude that each diamond−LN taper has a transmission efficiency of 92 ± 11% at 737 nm assuming equal taper and grating efficiencies (Figure 3b; see the Supporting Information for additional details on the calibration procedure). This high efficiency is visualized by the lack of significant scattering both at taper contact points to the TFLN and along the diamond nanobeam in Figure 3a. Importantly, grating couplers are very sensitive to the angle and focal plane of the incident light. Therefore, crosstalk and hysteresis in our stage motion can introduce an error into this efficiency calibration. However, additional repeated measurements across multiple thermal cycles yield similarly consistent values for taper efficiency. Furthermore, while this is the highest-efficiency device we measure, a second device exhibits an estimated single-taper transmission efficiency of greater than 80% (Supporting Information).

Optical Addressing of SiV Centers. We next perform photoluminescence (PL) measurements on SiV color centers embedded in the diamond nanobeam. There are two measurement configurations: one with the excitation and collection colocalized via the confocal path (C/C) and one with confocal excitation but collection through the grating couplers and transmission path (C/CP). Using a home-built confocal scanning microscope, we excite color centers off-resonantly at 710 nm and collect the ZPL emission at 737 nm. The resulting PL maps and spectra are presented in Figure 4a,b. After locating isolated bright spots in the PL, we sweep the optical excitation power and record the PL spectra, comparing the efficiency of SiV emission collected confocally to that collected through the integrated nanobeam channel. We toggle between confocal and grating coupler collection paths by removing the transmission path dichroic beamsplitter and adjusting only the half-wave plate just before the cryostat. We are careful to make minimal extraneous optical adjustments in order to maintain the validity of any comparisons of the collected signal.

From the PL spectra, we observe a small ensemble of emitters arising from the homogeneous distribution of SiVs throughout the diamond nanobeam. Therefore, for our specific device, we are unable to isolate a single emitter through off-resonant confocal excitation. To quantify photon extraction efficiencies, we measure PL spectra for different powers and integrate the signal within 6× the full width at half maximum (FWHM) of a representative transition for a SiV center, demarcated by gray in Figure 4b. We note that we select a transition that couples favorably to the diamond nanobeam. Figure 4c displays a fit to the saturation model $I(P) = I_\infty/(1 + P_{sat}/P)$. Errors for photon counts are given by assuming Poissonian photon statistics. From the best fit, we determine saturation powers P_{sat} of 6.9 ± 0.2 mW (9.8 ± 0.7 mW and 9.3 ± 0.7 mW) and saturation count rates I_∞ of 116 ± 2 kcps (68 ± 2 kcps and 219 ± 8 kcps) for the C/C configuration (C/CP$_1$ and C/CP$_2$). The difference in the signal between the two CP configurations can be attributed to preferential emission of the SiV in one direction of the nanobeam due to either angular dipole orientation or positioning in the nanobeam (see the Supporting Information). The discrepancy between C/C and C/CP saturation powers can in part be ascribed to polarization adjustments made between the configurations to optimize the power delivery to the color center with the removal of the second dichroic beamsplitter[41] (see the Supporting Information). This effect is expected to be pronounced due to the extreme polarization sensitivity of the dichroic beamsplitters at 710 nm. Additionally, the excitation and collection efficiencies of different color centers at the interrogated location depend strongly on the focus of the free space optics, as shown in the Supporting Information. Therefore, any misalignment in the focal plane for each configuration may contribute further to discrepancies in determined saturation powers. Given that there are inevitable adjustments made to alignment when switching between C/C and C/CP configurations, this may contribute further to discrepancies in power delivery efficiency.

Since we cannot collect data for powers $P \gg P_{\mathrm{sat}}$, we are unable to evaluate the impact of adding an additional background term to our saturation model fit. Hence, we estimate the enhancement factor for photon channeling into the TFLN waveguides by determining the signal ratio between the C/C and combined C/CP rates for the different measured powers and find an average enhancement factor of 2.05 ± 0.15.

As further evidence of emitter colocalization, we measure $g^{(2)}(\tau)$ autocorrelation of its emission in the C/C configuration using a 50:50 fiber beamsplitter. We isolate a single emission line with a series of filters (achieving roughly a 13 nm bandwidth at 740 nm; for more details, see the Supporting Information), and observe antibunching with $g^{(2)}(0) = 0.629 \pm 0.005$ for an excitation power of 4.74 mW, as shown in Figure 5a.

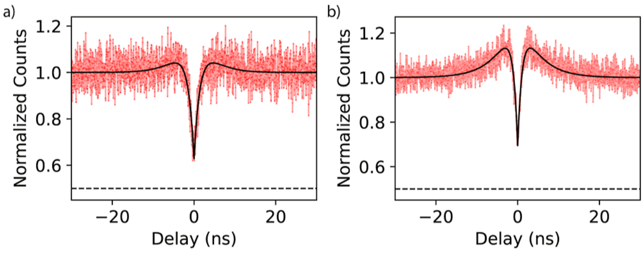

Figure 5. Photon autocorrelation measurements using confocal excitation and collected (a) confocally for an excitation power of 4.74 mW with $g^2(0) = 0.629 \pm 0.005$ and (b) through the grating coupler for an excitation power of 4.43 mW with $g^2(0) = 0.690 \pm 0.004$. The data are fitted using a bunched $g^2(\tau)$ function form, with counts far from the delay dip normalized to 1. The dashed line indicates the 0.5 threshold for single photon emitter characteristics. Error bars are calculated assuming Poissonian photon statistics.

We then repeat autocorrelation measurements in the C/CP configuration for an excitation power of 4.43 mW, utilizing our device as an integrated beamsplitter to correlate the emission between the two grating couplers. We measure a similar $g^{(2)}(0) = 0.690 \pm 0.004$ with this approach, as depicted in Figure 5b. The determined autocorrelation values at zero delay indicate emission from a small ensemble of emitters within our filtered wavelength region. This is consistent with the existence of additional peak and broadband background features shown in Figure 4b. We note that the bandwidth of our filter for the autocorrelation measurement is significantly larger than that imposed by postmeasurement data filtering in the saturation measurement. Therefore, the depth of the autocorrelation dip may be straightforwardly improved by increased spectral filtering.

Bunching in an autocorrelation measurement, observed for both C/C and C/CP configurations, is generally caused by telegraph noise due to either blinking or shelving into a long-lived metastable state. Since the degree of bunching depends on the excitation power,[42] the different degrees of bunching present for the two measurements are an additional indication of discrepancy in the power delivery efficiency for the two configurations, caused by the factors discussed above.

Lastly, we consider the robustness of the integration to environmental factors. It should be noted that this particular device survived multiple partial and complete thermal cycles. Furthermore, during one such event, the nanobeam fully detached from the TFLN waveguide socket and the pick-and-place apparatus is used to reposition the nanobeam. In all cases, we observed a similarly high transmission efficiency. Additional controlled thermal cycling and targeted testing will be necessary to formally characterize this robustness, but repeated transmission measurements suggest a lack of deterioration in the device performance.

■ DISCUSSION

Overall, we demonstrate the photonic integration of diamond color centers with TFLN. Our integration yields a high coupling efficiency of 92 ± 11% per facet between the diamond and the TFLN. We determine an enhancement factor between confocal collection and the combined rates of collecting through the TFLN grating couplers of 2.05 ± 0.15. Correcting for the determined grating coupler efficiency of 17.3 ± 1.2%, we estimate that channeling of SiV photons into the TFLN waveguide is improved by more than 10-fold when compared with that for out-of-plane confocal collection through a high-NA objective. A significant boost could be achieved by enhancing and channeling the color center emission through resonant photonic structures,[43,44] enabling an overall waveguide coupling efficiency of >60%.[14] Furthermore, for realistic applications, bidirectional emission from the color center can be channeled into a singular direction by adding a retroreflector or purposefully weakening the mirror strength on one side of a photonic resonator.

The emission count rate in our experiment is potentially limited by random placement and nonideal angular orientation of the SiV inside the nanobeam. The homogeneous distribution of color centers within the nanobeam also complicates the probing of single emitter properties in our device. These challenges can be overcome by delta doping and targeted implantation techniques, such as masked or focused ion beam implantation.[45−48]

A major advantage of selective integration is the possibility for large-scale precharacterization of diamond nanobeams and emitters, enabling a more deterministic device yield.[49] The transfer process could potentially be fully automated by using a combination of machine vision and in situ transmission measurements.

Our device paves the way for high-efficiency emitter collection on TFLN, enabling single-photon experiments that leverage TFLN's unique properties. We aim to utilize optical nonlinearities in LN for modulating color center emission, thereby demonstrating multiemitter interference and multiplexing on the chip.[50] We further aspire to add additional on-chip capabilities, such as on-chip filters[51] and detectors.[52,53] On-chip photon routing would enable both entanglement between several integrated quantum memories and coupling to the same external fiber channel. In combination with the recently demonstrated high fiber packaging efficiencies,[54] this would enable integrating a large number of quantum memories on the same chip. We also aim to leverage periodic poling in LN to achieve quantum frequency conversion of emitters to the infrared band for integration with telecommunication technologies. These future directions would pave the way toward on-chip heterogeneous platforms linking the excellent optical and coherence properties of solid-state spin qubits with the potential of a mature nonlinear photonics platform.

■ ASSOCIATED CONTENT

Data Availability Statement

All data are available from the authors upon reasonable request.

Supporting Information

The Supporting Information is available free of charge at https://pubs.acs.org/doi/10.1021/acsphotonics.3c00992.

> Additional information about the experimental setups, nanofabrication, calibration of measurements, autocorrelation measurements, and simulations of the device (PDF)

■ AUTHOR INFORMATION

Corresponding Authors

Daniel Riedel − *Edward L. Ginzton Lab, Stanford University, Stanford, California 94305, United States;* Present Address: AWS Center for Quantum Networking, Boston, Massachusetts 02210, United States; orcid.org/0000-0001-8058-6993; Email: riedeld@stanford.edu

Jelena Vučković − *Edward L. Ginzton Lab, Stanford University, Stanford, California 94305, United States;* orcid.org/0000-0002-4603-9686; Email: jela@stanford.edu

Authors

Hope Lee − *Edward L. Ginzton Lab, Stanford University, Stanford, California 94305, United States;* orcid.org/0000-0003-3043-3459

Jason F. Herrmann − *Edward L. Ginzton Lab, Stanford University, Stanford, California 94305, United States*

Jakob Grzesik − *Edward L. Ginzton Lab, Stanford University, Stanford, California 94305, United States*

Vahid Ansari − *Edward L. Ginzton Lab, Stanford University, Stanford, California 94305, United States*

Jean-Michel Borit − *Edward L. Ginzton Lab, Stanford University, Stanford, California 94305, United States*

Hubert S. Stokowski − *Edward L. Ginzton Lab, Stanford University, Stanford, California 94305, United States;* orcid.org/0000-0001-6416-9639

Shahriar Aghaeimeibodi − *Edward L. Ginzton Lab, Stanford University, Stanford, California 94305, United States;* Present Address: AWS Center for Quantum Computing, San Francisco, California 94105, United States.; orcid.org/0000-0002-9920-493X

Haiyu Lu − *Edward L. Ginzton Lab, Stanford University, Stanford, California 94305, United States*

Patrick J. McQuade − *Edward L. Ginzton Lab, Stanford University, Stanford, California 94305, United States*

Nicholas A. Melosh − *Edward L. Ginzton Lab, Stanford University, Stanford, California 94305, United States;* orcid.org/0000-0002-2601-1379

Zhi-Xun Shen − *Edward L. Ginzton Lab, Stanford University, Stanford, California 94305, United States*

Amir H. Safavi-Naeini − *Edward L. Ginzton Lab, Stanford University, Stanford, California 94305, United States*

Complete contact information is available at: https://pubs.acs.org/10.1021/acsphotonics.3c00992

Author Contributions

D.R., H.Lee, J.F.H., and J.G. contributed equally to this work. H.Lee, J.G., and D.R. contributed to the diamond nanobeam design and fabrication. H.Lu, P.J.M., N.A.M. and Z.X.S., contributed to the diamond sample growth and material preparation. TFLN grating couplers were designed by J.F.H., and J.F.H. and V.A. contributed to the TFLN chip fabrication. The adiabatic taper was initially designed and simulated by J.M.B., D.R., and S.A., with follow-up simulations conducted by J.M.B., D.R., and J.F.H. The pick and place setup and transfer of the diamond nanobeam to TFLN was carried out by H.Lee, D.R., and J.G. Optical measurements of the integrated device were led by H. Lee and assisted by D.R., J.G., and J.F.H. The manuscript was prepared by H.Lee, J.F.H., J.G., and D.R. Additional support and assistance were provided by H.S.S., A.H.S.N., and J.V. A.H.S.N. and J.V. oversaw the experiment and assisted in the data interpretation and editing of the manuscript.

Notes

The authors declare no competing financial interest.

During the writing of this paper, we learned of work using similar techniques to calibrate for the transmission efficiencies of adiabatic tapers in a different material platform.[55]

■ ACKNOWLEDGMENTS

This material is based upon work supported by the U.S. Department of Energy Office of Science National Quantum Information Science Research Centers as part of the Q-NEXT center. H. Lee acknowledges support from the Stanford Graduate Fellowship. J.F.H. acknowledges support from the NSF GRFP under grant no. DGE-1656518. J.G. acknowledges support from the Hertz Foundation Graduate Fellowship. S.A. and V.A. acknowledge support from the Bloch postdoctoral fellowship in quantum science and engineering from the Stanford Quantum Fundamentals, Architecture, and Machines initiative (Q-FARM). D.R. acknowledges support from the Swiss National Science Foundation (project no. P400P2_194424). D.R. and S.A. contributed to this work prior to joining AWS. H.S.S. acknowledges support from the Urbanek Family Fellowship. H. Lu and Z.X.S. were supported by the DOE Office of Basic Energy Sciences, Division of Materials Science and Engineering. The authors thank Patrick McQuade and Alison Rugar for assistance with the diamond sample growth. The authors thank Daniil Lukin, Samuel Gyger, Eric Irving Rosenthal, and Luke Qi for helpful discussions regarding sample measurements and data analysis. Work was performed in part in the nano@Stanford laboratories, which are supported by the National Science Foundation as part of the National Nanotechnology Coordinated Infrastructure under award ECCS-2026822. Part of this work was performed at the Stanford Nano Shared Facilities (SNSF), supported by the National Science Foundation under award ECCS-2026822.

■ REFERENCES

(1) Awschalom, D. D.; Hanson, R.; Wrachtrup, J.; Zhou, B. B. Quantum technologies with optically interfaced solid-state spins. *Nat. Photonics* **2018**, *12*, 516−527.

(2) Atatüre, M.; Englund, D.; Vamivakas, N.; Lee, S.-Y.; Wrachtrup, J. Material platforms for spin-based photonic quantum technologies. *Nat. Rev. Mater.* **2018**, *3*, 38−51.

(3) Abobeih, M. H.; Wang, Y.; Randall, J.; Loenen, S. J.; Bradley, C. E.; Markham, M.; Twitchen, D. J.; Terhal, B. M.; Taminiau, T. H. Fault-tolerant operation of a logical qubit in a diamond quantum processor. *Nature* **2022**, *606*, 884−889.

(4) Bradley, C. E.; Randall, J.; Abobeih, M. H.; Berrevoets, R. C.; Degen, M. J.; Bakker, M. A.; Markham, M.; Twitchen, D. J.; Taminiau, T. H. A Ten-Qubit Solid-State Spin Register with Quantum Memory up to One Minute. *Phys. Rev. X* **2019**, *9*, 031045.

(5) Pompili, M.; Hermans, S. L. N.; Baier, S.; Beukers, H. K. C.; Humphreys, P. C.; Schouten, R. N.; Vermeulen, R. F. L.; Tiggelman, M. J.; dos Santos Martins, L.; Dirkse, B.; Wehner, S.; Hanson, R. Realization of a multinode quantum network of remote solid-state qubits. *Science* **2021**, *372*, 259−264.

(6) Hermans, S. L. N.; Pompili, M.; Beukers, H. K. C.; Baier, S.; Borregaard, J.; Hanson, R. Qubit teleportation between non-neighbouring nodes in a quantum network. *Nature* **2022**, *605*, 663−668.

(7) Faraon, A.; Santori, C.; Huang, Z.; Acosta, V. M.; Beausoleil, R. G. Coupling of nitrogen-vacancy centers to photonic crystal cavities in monocrystalline diamond. *Phys. Rev. Lett.* **2012**, *109*, 033604.

(8) Riedel, D.; Söllner, I.; Shields, B. J.; Starosielec, S.; Appel, P.; Neu, E.; Maletinsky, P.; Warburton, R. J. Deterministic Enhancement of Coherent Photon Generation from a Nitrogen-Vacancy Center in Ultrapure Diamond. *Phys. Rev. X* **2017**, *7*, 031040.

(9) Orphal-Kobin, L.; Unterguggenberger, K.; Pregnolato, T.; Kemf, N.; Matalla, M.; Unger, R.-S.; Ostermay, I.; Pieplow, G.; Schröder, T. Optically Coherent Nitrogen-Vacancy Defect Centers in Diamond Nanostructures. *Phys. Rev. X* **2023**, *13*, 011042.

(10) Evans, R. E.; Sipahigil, A.; Sukachev, D. D.; Zibrov, A. S.; Lukin, M. D. Narrow-Linewidth Homogeneous Optical Emitters in Diamond Nanostructures via Silicon Ion Implantation. *Phys. Rev. Appl.* **2016**, *5*, 044010.

(11) Rugar, A. E.; Dory, C.; Aghaeimeibodi, S.; Lu, H.; Sun, S.; Mishra, S. D.; Shen, Z.-X.; Melosh, N. A.; Vučković, J. Narrow-Linewidth Tin-Vacancy Centers in a Diamond Waveguide. *ACS Photonics* **2020**, *7*, 2356−2361.

(12) Thiering, G.; Gali, A. Ab Initio Magneto-Optical Spectrum of Group-IV Vacancy Color Centers in Diamond. *Phys. Rev. X* **2018**, *8*, 021063.

(13) Bhaskar, M. K.; Riedinger, R.; Machielse, B.; Levonian, D. S.; Nguyen, C. T.; Knall, E. N.; Park, H.; Englund, D.; Lončar, M.; Sukachev, D. D.; Lukin, M. D. Experimental demonstration of memory-enhanced quantum communication. *Nature* **2020**, *580*, 60−64.

(14) Knall, E. N.; Knaut, C.; Bekenstein, R.; Assumpcao, D.; Stroganov, P.; Gong, W.; Huan, Y.; Stas, P. J.; Machielse, B.; Chalupnik, M.; et al. Efficient Source of Shaped Single Photons Based on an Integrated Diamond Nanophotonic System. *Phys. Rev. Lett.* **2022**, *129*, 053603.

(15) Wan, N. H.; Lu, T.-J.; Chen, K. C.; Walsh, M. P.; Trusheim, M. E.; De Santis, L.; Bersin, E. A.; Harris, I. B.; Mouradian, S. L.; Christen, I. R.; Bielejec, E. S.; Englund, D. Large-scale integration of artificial atoms in hybrid photonic circuits. *Nature* **2020**, *583*, 226−231.

(16) Xuan, Y.; Liu, Y.; Varghese, L. T.; Metcalf, A. J.; Xue, X.; Wang, P. H.; Han, K.; Jaramillo-Villegas, J. A.; Al Noman, A.; Wang, C.; et al. High-Q silicon nitride microresonators exhibiting low-power frequency comb initiation. *Optica* **2016**, *3*, 1171.

(17) Lu, X.; Li, Q.; Westly, D. A.; Moille, G.; Singh, A.; Anant, V.; Srinivasan, K. Chip-integrated visible−telecom entangled photon pair source for quantum communication. *Nat. Phys.* **2019**, *15*, 373−381.

(18) Elshaari, A. W.; Pernice, W.; Srinivasan, K.; Benson, O.; Zwiller, V. Hybrid integrated quantum photonic circuits. *Nat. Photonics* **2020**, *14*, 285−298.

(19) Kim, J. H.; Aghaeimeibodi, S.; Carolan, J.; Englund, D.; Waks, E. Hybrid integration methods for on-chip quantum photonics. *Optica* **2020**, *7*, 291.

(20) Lake, D. P.; Mitchell, M.; Jayakumar, H.; dos Santos, L. F.; Curic, D.; Barclay, P. E. Efficient telecom to visible wavelength conversion in doubly resonant gallium phosphide microdisks. *Appl. Phys. Lett.* **2016**, *108*, 031109.

(21) Wilson, D. J.; Schneider, K.; Hönl, S.; Anderson, M.; Baumgartner, Y.; Czornomaz, L.; Kippenberg, T. J.; Seidler, P. Integrated gallium phosphide nonlinear photonics. *Nat. Photonics* **2020**, *14*, 57−62.

(22) Jung, H.; Yu, S.-P.; Carlson, D. R.; Drake, T. E.; Briles, T. C.; Papp, S. B. Tantala Kerr nonlinear integrated photonics. *Optica* **2021**, *8*, 811.

(23) Guidry, M. A.; Yang, K. Y.; Lukin, D. M.; Markosyan, A.; Yang, J.; Fejer, M. M.; Vučković, J. Optical parametric oscillation in silicon carbide nanophotonics. *Optica* **2020**, *7*, 1139.

(24) Wang, C.; Fang, Z.; Yi, A.; Yang, B.; Wang, Z.; Zhou, L.; Shen, C.; Zhu, Y.; Zhou, Y.; Bao, R.; et al. High-Q microresonators on 4H-silicon-carbide-on-insulator platform for nonlinear photonics. *Light: Sci. Appl.* **2021**, *10*, 139.

(25) Wu, R.; Zhang, J.; Yao, N.; Fang, W.; Qiao, L.; Chai, Z.; Lin, J.; Cheng, Y. Lithium niobate micro-disk resonators of quality factors above 107. *Opt. Lett.* **2018**, *43*, 4116.

(26) Zhu, D.; Shao, L.; Yu, M.; Cheng, R.; Desiatov, B.; Xin, C. J.; Hu, Y.; Holzgrafe, J.; Ghosh, S.; Shams-Ansari, A.; Puma, E.; Sinclair, N.; Reimer, C.; Zhang, M.; Lončar, M. Integrated photonics on thin-film lithium niobate. *Adv. Opt. Photonics* **2021**, *13*, 242.

(27) Wang, C.; Zhang, M.; Stern, B.; Lipson, M.; Lončar, M. Nanophotonic lithium niobate electro-optic modulators. *Opt. Express* **2018**, *26*, 1547−1555.

(28) Zhang, M.; Wang, C.; Kharel, P.; Zhu, D.; Lončar, M. Integrated lithium niobate electro-optic modulators: when performance meets scalability. *Optica* **2021**, *8*, 652−667.

(29) McKenna, T. P.; Witmer, J. D.; Patel, R. N.; Jiang, W.; Van Laer, R.; Arrangoiz-Arriola, P.; Wollack, E. A.; Herrmann, J. F.; Safavi-Naeini, A. H. Cryogenic microwave-to-optical conversion using a triply resonant lithium-niobate-on-sapphire transducer. *Optica* **2020**, *7*, 1737−1745.

(30) Holzgrafe, J.; Sinclair, N.; Zhu, D.; Shams-Ansari, A.; Colangelo, M.; Hu, Y.; Zhang, M.; Berggren, K. K.; Lončar, M. Cavity electro-optics in thin-film lithium niobate for efficient microwave-to-optical transduction. *Optica* **2020**, *7*, 1714−1720.

(31) Jiang, W.; Patel, R. N.; Mayor, F. M.; McKenna, T. P.; Arrangoiz-Arriola, P.; Sarabalis, C. J.; Witmer, J. D.; Van Laer, R.; Safavi-Naeini, A. H. Lithium niobate piezo-optomechanical crystals. *Optica* **2019**, *6*, 845−853.

(32) Jiang, W.; Mayor, F. M.; Malik, S.; Van Laer, R.; McKenna, T. P.; Patel, R. N.; Witmer, J. D.; Safavi-Naeini, A. H. Optically heralded microwave photon addition. *Nat. Phys.* **2023**, *19*, 1423−1428.

(33) McKenna, T. P.; Stokowski, H. S.; Ansari, V.; Mishra, J.; Jankowski, M.; Sarabalis, C. J.; Herrmann, J. F.; Langrock, C.; Fejer, M. M.; Safavi-Naeini, A. H. Ultra-low-power second-order nonlinear optics on a chip. *Nat. Commun.* **2022**, *13*, 4532.

(34) Park, T.; Stokowski, H. S.; Ansari, V.; McKenna, T. P.; Hwang, A. Y.; Fejer, M.; Safavi-Naeini, A. H. High-efficiency second harmonic generation of blue light on thin-film lithium niobate. *Opt. Lett.* **2022**, *47*, 2706−2709.

(35) Mouradian, S.; Wan, N. H.; Schröder, T.; Englund, D. Rectangular photonic crystal nanobeam cavities in bulk diamond. *Appl. Phys. Lett.* **2017**, *111*, 021103.

(36) Zhu, Y.; Wei, W.; Yi, A.; Jin, T.; Shen, C.; Wang, X.; Zhou, L.; Wang, C.; Ou, W.; Song, S.; Wang, T.; Zhang, J.; Ou, X.; Zhang, J. Hybrid Integration of Deterministic Quantum Dot-Based Single-Photon Sources with CMOS-Compatible Silicon Carbide Photonics. *Laser Photonics Rev.* **2022**, *16*, 2200172.

(37) Chanana, A.; Larocque, H.; Moreira, R.; Carolan, J.; Guha, B.; Melo, E. G.; Anant, V.; Song, J.; Englund, D.; Blumenthal, D. J.; Srinivasan, K.; Davanco, M. Ultra-low loss quantum photonic circuits integrated with single quantum emitters. *Nat. Commun.* **2022**, *13*, 7693.

(38) Xie, L.; Zhou, T. X.; Stöhr, R. J.; Yacoby, A. Crystallographic Orientation Dependent Reactive Ion Etching in Single Crystal Diamond. *Adv. Mater.* **2018**, *30*, 1705501.

(39) Khanaliloo, B.; Mitchell, M.; Hryciw, A. C.; Barclay, P. E. High-Q/V Monolithic Diamond Microdisks Fabricated with Quasi-isotropic Etching. *Nano Lett.* **2015**, *15*, 5131−5136.

(40) Khanaliloo, B.; Jayakumar, H.; Hryciw, A. C.; Lake, D. P.; Kaviani, H.; Barclay, P. E. Single-Crystal Diamond Nanobeam Waveguide Optomechanics. *Phys. Rev. X* **2015**, *5*, 041051.

(41) Mouradian, S. L.; Schröder, T.; Poitras, C. B.; Li, L.; Goldstein, J.; Chen, E. H.; Walsh, M.; Cardenas, J.; Markham, M. L.; Twitchen, D. J.; Lipson, M.; Englund, D. Scalable Integration of Long-Lived Quantum Memories into a Photonic Circuit. *Phys. Rev. X* **2015**, *5*, 031009.

(42) Neu, E.; Steinmetz, D.; Riedrich-Möller, J.; Gsell, S.; Fischer, M.; Schreck, M.; Becher, C. Single photon emission from silicon-vacancy colour centres in chemical vapour deposition nano-diamonds on iridium. *New J. Phys.* **2011**, *13*, 025012.

(43) Rugar, A. E.; Aghaeimeibodi, S.; Riedel, D.; Dory, C.; Lu, H.; McQuade, P. J.; Shen, Z.-X.; Melosh, N. A.; Vučković, J. Quantum Photonic Interface for Tin-Vacancy Centers in Diamond. *Phys. Rev. X* **2021**, *11*, 031021.

(44) Nguyen, C. T.; Sukachev, D. D.; Bhaskar, M. K.; Machielse, B.; Levonian, D. S.; Knall, E. N.; Stroganov, P.; Riedinger, R.; Park, H.; Lončar, M.; Lukin, M. D. Quantum Network Nodes Based on Diamond Qubits with an Efficient Nanophotonic Interface. *Phys. Rev. Lett.* **2019**, *123*, 183602.

(45) Nguyen, C. T.; Sukachev, D. D.; Bhaskar, M. K.; Machielse, B.; Levonian, D. S.; Knall, E. N.; Stroganov, P.; Chia, C.; Burek, M. J.; Riedinger, R.; Park, H.; Lončar, M.; Lukin, M. D. An integrated nanophotonic quantum register based on silicon-vacancy spins in diamond. *Phys. Rev. B* **2019**, *100*, 165428.

(46) Rugar, A. E.; Lu, H.; Dory, C.; Sun, S.; McQuade, P. J.; Shen, Z.-X.; Melosh, N. A.; Vučković, J. Generation of Tin-Vacancy Centers in Diamond via Shallow Ion Implantation and Subsequent Diamond Overgrowth. *Nano Lett.* **2020**, *20*, 1614−1619.

(47) Schröder, T.; Trusheim, M. E.; Walsh, M.; Li, L.; Zheng, J.; Schukraft, M.; Sipahigil, A.; Evans, R. E.; Sukachev, D. D.; Nguyen, C. T.; Pacheco, J. L.; Camacho, R. M.; Bielejec, E. S.; Lukin, M. D.; Englund, D. Scalable focused ion beam creation of nearly lifetime-limited single quantum emitters in diamond nanostructures. *Nat. Commun.* **2017**, *8*, 15376.

(48) Titze, M.; Byeon, H.; Flores, A.; Henshaw, J.; Harris, C. T.; Mounce, A. M.; Bielejec, E. S. In Situ Ion Counting for Improved Implanted Ion Error Rate and Silicon Vacancy Yield Uncertainty. *Nano Lett.* **2022**, *22*, 3212−3218.

(49) Sutula, M.; Christen, I.; Bersin, E.; Walsh, M. P.; Chen, K. C.; Mallek, J.; Melville, A.; Titze, M.; Bielejec, E. S.; Hamilton, S.; Braje, D.; Dixon, P. B.; Englund, D. R. Large-scale optical characterization of solid-state quantum emitters. *Nat. Mater.* **2023**, *22*, 1338−1344.

(50) Narita, Y.; Wang, P.; Ikeda, K.; Oba, K.; Miyamoto, Y.; Taniguchi, T.; Onoda, S.; Hatano, M.; Iwasaki, T. Multiple Tin-Vacancy Centers in Diamond with Nearly Identical Photon Frequency and Linewidth. *Phys. Rev. Appl.* **2023**, *19*, 024061.

(51) Elshaari, A. W.; Zadeh, I. E.; Fognini, A.; Reimer, M. E.; Dalacu, D.; Poole, P. J.; Zwiller, V.; Jöns, K. D. On-chip single photon filtering and multiplexing in hybrid quantum photonic circuits. *Nat. Commun.* **2017**, *8*, 379.

(52) Reithmaier, G.; Kaniber, M.; Flassig, F.; Lichtmannecker, S.; Müller, K.; Andrejew, A.; Vučković, J.; Gross, R.; Finley, J. J. On-Chip Generation, Routing, and Detection of Resonance Fluorescence. *Nano Lett.* **2015**, *15*, 5208−5213.

(53) Najafi, F.; Mower, J.; Harris, N. C.; Bellei, F.; Dane, A.; Lee, C.; Hu, X.; Kharel, P.; Marsili, F.; Assefa, S.; Berggren, K. K.; Englund, D. On-chip detection of non-classical light by scalable integration of single-photon detectors. *Nat. Commun.* **2015**, *6*, 5873.

(54) Zeng, B.; De-Eknamkul, C.; Assumpcao, D.; Renaud, D.; Wang, Z.; Riedel, D.; Ha, J.; Robens, C.; Levonian, D.; Lukin, M.; Riedinger, R.; Bhaskar, M.; Sukachev, D.; Loncar, M.; et al. Cryogenic packaging of nanophotonic devices with a low coupling loss <1 dB. *Appl. Phys. Lett.* **2023**, *123*, 161106.

(55) Larocque, H.; Buyukkaya, M. A.; Errando-Herranz, C.; Harper, S.; Carolan, J.; Lee, C.-M.; Richardson, C. J. K.; Leake, G. L.; Coleman, D. J.; Fanto, M. L.; Waks, E.; Englund, D. Tunable quantum emitters on large-scale foundry silicon photonics. **2023**, arXiv:2306.06460. 10 June 2023 (accessed 2022-11-09).

https://doi.org/10.1021/acsphotonics.3c00992